



Plasma-Sprayed High-Performance $(\text{Bi}_2\text{O}_3)_{0.75}(\text{Y}_2\text{O}_3)_{0.25}$ Electrolyte for Intermediate-Temperature Solid Oxide Fuel Cells (IT-SOFCs)

Rui Chen¹ · Shan-Lin Zhang¹ · Chang-Jiu Li¹ · Cheng-Xin Li¹

Submitted: 3 September 2020 / in revised form: 6 January 2021 / Accepted: 12 January 2021 / Published online: 28 January 2021
© ASM International 2021

Abstract Rare earth element-doped bismuth oxides with the fluorite structure ($\delta\text{-Bi}_2\text{O}_3$) exhibit high oxygen ion conductivity at low temperature, which is promising electrolyte materials for intermediate-temperature solid oxide fuel cells (IT-SOFCs). However, traditional co-sintering process is not applicable to the manufacturing of IT-SOFCs using low melting point Bi_2O_3 -based electrolyte, while further high-temperature processing is not required for deposition Bi_2O_3 -based electrolytes. In this study, plasma spraying was used to examine the possibility to deposit high-performance Bi_2O_3 -based electrolytes without the following high-temperature process. $(\text{Bi}_2\text{O}_3)_{0.75}(\text{Y}_2\text{O}_3)_{0.25}$ (YSB) spray powders were prepared by the sinter-crushing method. The YSB electrolytes were fabricated by plasma spraying at different deposition temperatures. The effects of deposition temperature on the coating microstructure, crystalline stability, and ion conductivity were investigated. Results showed that the as-sprayed YSB electrolytes present a dense microstructure with well-bonded lamellar interfaces. The pure δ -phase YSB electrolyte was deposited with 37.5–75 μm powders at a deposition temperature of 350 °C. The deposited YSB electrolyte presented the

excellent ionic conductivity of 0.19 S cm^{-1} at 700 °C in comparison with 0.21 S cm^{-1} for sintered bulk.

Keywords conductivity · IT-SOFC · plasma spraying · YSB electrolyte

Introduction

Solid oxide fuel cell (SOFC) is one of the cleanest and most efficient energy conversion devices. The device directly converts the chemical energy of a fuel to electrical energy by an electrochemical reaction overcoming combustion efficiency limitations (e.g., the Carnot cycle). The energy conversion efficiency of the stand-alone SOFC device can be 45% up to 65% which is twice that of internal combustion engines (Ref 1). SOFCs have three major components, two porous electrodes (anode and cathode) and one dense electrolyte that separates the two electrodes. The oxygen gas from air is reduced at the cathode, and oxygen ions are transported to the anode side where they react with fuel releasing electrons to the external circuit. The key issue for the commercialization and the applications of SOFCs is the high operating temperature, resulting in materials and cost limitations and operating complexities (Ref 2). It is necessary to develop efficient electrolyte materials of higher ionic conductivity at lower temperatures to reduce the operating temperature of SOFCs. The bismuth oxide materials are potential electrolytes for the intermediate-temperature solid oxide fuel cells (IT-SOFCs) because of their excellent oxygen ionic conductivity at intermediate temperatures.

Bismuth oxides with defect fluorite-type lattice contain a large concentration of oxygen vacancies (1/4) (Ref 3). The defect fluorite-type lattice of high oxygen concentration

This article is an invited paper selected from abstracts submitted for the 2020 International Thermal Spray Conference, ITSC2020, that was to be held from June 10 to June 12, 2020, in Vienna, Austria. The conference was canceled due to the coronavirus (COVID-19) pandemic. The paper has been expanded from the planned presentation.

✉ Chang-Jiu Li
licj@mail.xjtu.edu.cn

¹ State Key Laboratory for Mechanical Behavior of Materials, School of Materials Science and Engineering, Xi'an Jiaotong University, Xi'an 710049, Shaanxi, People's Republic of China

makes bismuth oxide exhibit the highest ionic conductivity among ionic conductive oxides. Thus, the ionic conductivity of pure $\delta\text{-Bi}_2\text{O}_3$ (1.00 S cm^{-1}) (Ref 4) is significantly higher than traditional electrolyte material, such as yttria-stabilized zirconia (YSZ, $5.1 \times 10^{-3}\text{ S cm}^{-1}$) (Ref 5) at 650 °C. Therefore, bismuth oxides can be considered as high potential electrolyte materials for IT-SOFCs to reduce the operating temperature, which is expected to reduce cell degradation rates, e.g., by reducing Cr volatilization from interconnectors (Ref 6).

However, pure $\delta\text{-Bi}_2\text{O}_3$ electrolyte is only stable in a narrow high temperature range (Ref 7). As shown in Table 1, $\delta\text{-Bi}_2\text{O}_3$ transforms to body-centered cubic γ -phase, tetragonal β -phase, and monoclinic α -phase at a temperature below 730 °C, accompanying the change of volume and a significant decrease in conductivity (Ref 8). As reported in previous studies, the doped bismuth oxides with various rare earth oxides such as Dy_2O_3 (Ref 9), Er_2O_3 (Ref 10), Y_2O_3 (Ref 11), Yb_2O_3 (Ref 12), and Ta_2O_5 (Ref 13) maintain the high-temperature δ -phase at room temperature. Among these materials, considering the economic issues, Y_2O_3 -stabilized Bi_2O_3 with excellent ionic conductivity at intermediate temperatures was used in this study. As reported by Takahashi et al. (Ref 14), Y_2O_3 -stabilized Bi_2O_3 is stable at a concentration range of 25-43 mol% Y_2O_3 . 25 mol% Y_2O_3 -stabilized Bi_2O_3 exhibits the highest ionic conductivity, e.g., 25 mol% Y_2O_3 -stabilized Bi_2O_3 (YSB) exhibiting ionic conductivity of $1.6 \times 10^{-1}\text{ S cm}^{-1}$ at 700 °C and $1.2 \times 10^{-2}\text{ S cm}^{-1}$ at 500 °C, which are 1-2 orders higher in magnitude than YSZ electrolyte (e.g., $1.1 \times 10^{-2}\text{ S cm}^{-1}$ at 700 °C, $4.0 \times 10^{-4}\text{ S cm}^{-1}$ at 500 °C) (Ref 4).

The low melting point of bismuth oxide (825 °C) significantly restricts the high-temperature co-sintering steps during the manufacturing of SOFCs, since with the conventional electrolyte fabrication processes of SOFCs such as screen printing (Ref 15), sol-gel (Ref 16), and dip coating (Ref 17), the co-sintering temperature is generally in a range of 1000-1200 °C during the following cathode fabricated process (Ref 18). Accordingly, at present, various low-temperature fabrication processes have been developed for the deposition of bismuth oxide electrolyte films such as vapor deposition (Ref 19), direct current (DC) magnetron sputtering (Ref 20), and pulsed laser deposition

(PLD) (Ref 21) to avoid this issue. However, those processes have disadvantages like being complicated, having high manufacturing costs, or low efficiency, which limits the commercialization of IT-SOFCs.

Compared with the above-mentioned processes, atmospheric plasma spraying (APS) has been developed and used for cost-effective fabrication of IT-SOFCs because APS is a proven usable, low-cost, large-scalable industrial production process. Zhang et al. have successfully prepared YSZ (Ref 22) and $\text{La}_{0.8}\text{Sr}_{0.2}\text{Ga}_{0.8}\text{Mg}_{0.2}\text{O}_{3-\delta}$ (LSGM) (Ref 23) by APS with excellent performance and can be applied directly to SOFC electrolytes. For the bismuth-based electrolyte in SOFC, the deposit prepared by APS is required to have a dense microstructure with a stable δ -phase. Comparing with a sintered bulk electrolyte, the deposit prepared by APS generally presents a lamellar structure. The thermally sprayed ceramic deposit may exhibit poor conductive performance due to the limited interface bonding. The recent investigation revealed that the deposition temperature during spraying plays a significant role in the formation of interlamellar bonding (Ref 24). It has been found that there is a critical bonding temperature for certain ceramic coating material over which ceramic splat will bond to the previously deposited splats during splatting (Ref 25). Moreover, it was found that the critical bonding temperature nearly linearly increases with the melting point of the spray material (Ref 26). Accordingly, based on the above theory, a dense coating with fully bonded lamellae can be fabricated by APS at room deposition temperature for the ceramic material with a melting point lower than about 1500 °C (Ref 27). Since the melting point of a doped Bi_2O_3 is lower than 1000 °C, it can be rationally considered based on our previous findings that a dense YSB electrolyte for IT-SOFC can be prepared by plasma spraying.

It is well known that the sintered YSB bulk with stable $\delta\text{-Bi}_2\text{O}_3$ exhibits high ionic conductivity, while the conductivity of doped $\delta\text{-Bi}_2\text{O}_3$ phase depends on the dopant concentration (Ref 14). On the other hand, the recent investigation revealed that the composition of the ceramic deposit consisting of multiple components by plasma spraying may deviate from its starting powder (Ref 23, 28-30). Since YSB consists of Y_2O_3 and Bi_2O_3 which have different vapor pressures, Bi_2O_3 may vaporize

Table 1 Conductivities of different phases of Bi_2O_3 (Ref 8)

Phase	Existence domain, °C	Conductivity at 600°C, S cm^{-1}	Conductivity at 650°C, S cm^{-1}
$\delta\text{-Bi}_2\text{O}_3$	>730	...	~ 1
$\gamma\text{-Bi}_2\text{O}_3$	650 down to 600	~ 3×10^{-3}	~ 5×10^{-3}
$\beta\text{-Bi}_2\text{O}_3$	648 down to 500 500 up to 663	~ 10^{-3}	~ 2×10^{-3}
$\alpha\text{-Bi}_2\text{O}_3$	0 up to 730	10^{-4}	~ 3×10^{-4}

preferentially during plasma spraying to alter the composition of YSB deposits. This change subsequently influences the stability of the δ - Bi_2O_3 phase in the deposit. However, no result concerning with the phase transition of YSB electrolyte fabricated by APS involving rapid heating to melting and subsequently rapid quenching processes was reported in the literature yet.

Therefore, YSB spray powders were synthesized by a solid state reaction process and YSB electrolyte was deposited by plasma spraying to investigate the microstructural features of APS YSB and the effect of the deposition temperature on the microstructure, crystal structure, and ion conductivity in this study.

Experimentals

Materials and Deposition Methods

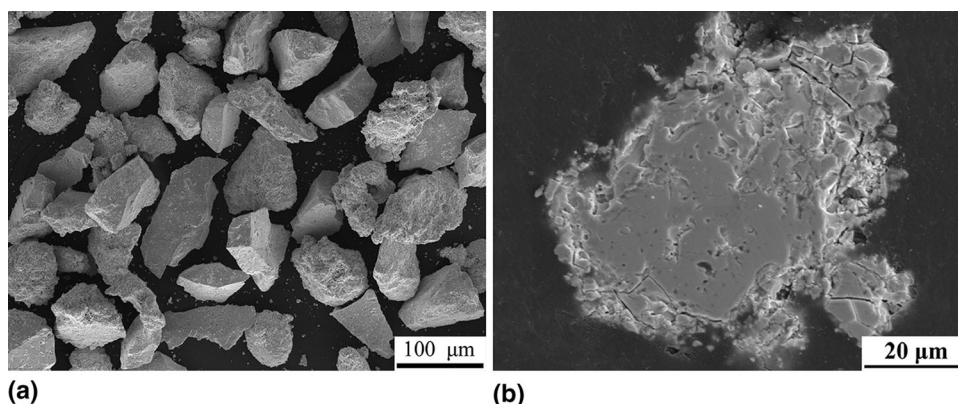
25 mol% Y_2O_3 -doped Bi_2O_3 spray powder was synthesized by the sinter-crushing method. Nanosized Y_2O_3 (99.9% purity, Ningbo Begaer) and Bi_2O_3 (99.99% purity, Ningbo Begaer) powders were used as the starting materials. Stoichiometric amounts of the powders were ball-milled in ethanol for 20 hours with zirconia balls as a milling medium. The mixed powders were dried and ground in an agate mortar. Then, 5 wt.% polyvinyl alcohol solution was added into the mixed powders to enhance the binding between the powder particles. The dried powders were reground and sieved through a 200-mesh screen. The mixed powders were calcined in air at 800 °C for 24 h to obtain the YSB powders. The powders used for the plasma spraying were sieved through 200 and 400 meshes to select the powders of a size range from 37.5 to 75 μm , since the previous results revealed that using large powder particles may suppress the composition change of plasma-sprayed YSB with respect to the starting powders (Ref 23, 29, 30).

Figure 1 shows the SEM morphology and cross-sectional microstructure of synthesized YSB powder. The

powder shows an irregular shape with a dense structure although some small pores are present in the powder. Figure 2 shows the XRD pattern of YSB powders. The XRD pattern reveals that only a single cubic fluorite phase (δ -phase) with the Fm-3m space group (PDF #40-0320) was observed. There were no peaks of low-temperature monoclinic α - Bi_2O_3 and metastable tetragonal β - Bi_2O_3 , body-centered cubic γ - Bi_2O_3 phases. This fact indicates that 25% Y_2O_3 doped Bi_2O_3 powders calcined at 800 °C by the sinter-crushing synthesis method present the stable crystal δ -phase.

Plasma spray parameters are given in Table 2. A commercial plasma spray system (ZB-80, Beijing, China) was used for YSB electrolyte deposition. Ar as the primary plasma gas and H_2 as an auxiliary plasma gas were used to generate high-temperature plasma jet. The plasma spraying was performed at a plasma arc power of 25 kW in the present study based on the preliminary experiments to acquire sufficiently molten YSB particles. The deposition temperature, which is defined as the surface temperature of the substrate prior molten droplet impact during spraying, was controlled through a special heating plate. The substrate was made contact with the plate by a fixture during spraying. Before spraying the substrate temperature is preheated to the pre-determined temperature by the heating plate. NaCl pellets with a diameter of 20 mm and a thickness of 2 mm were used as the substrate. An infrared pyrometer (RayRPM30L3U, Raytek, America) with 8–14 μm wavelength and 0.82 emissivity (Ref 31) was used to monitor the surface temperature of the NaCl substrate. To investigate the effect of the deposition temperature on the phase structure and microstructure, the YSB was deposited at two deposition temperatures, i.e., room temperature and 350 °C. The plasma torch traverse speed over the substrate was 400 mm/s. The deposited samples were soaked in water to remove the substrate and obtain the free-standing YSB deposits. The bulk 25YSB pellet was also fabricated by sintering the pressed green pellet in air at 800 °C for 10 h for the measurement of ion conductivity.

Fig. 1 (a) Morphology of YSB powders; (b) cross-sectional morphology of YSB powder



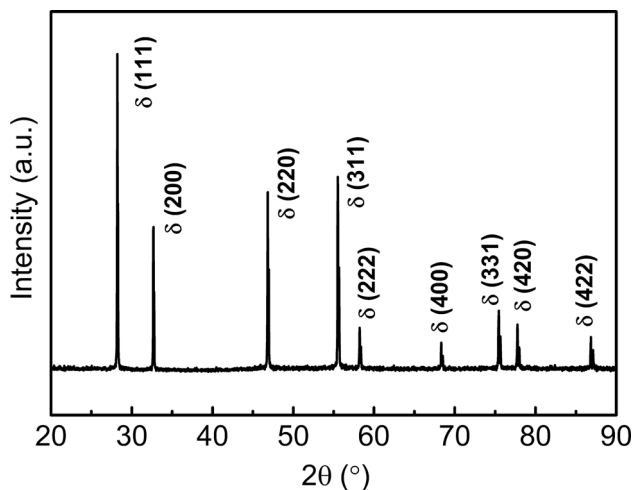


Fig. 2 XRD pattern of YSB powder used for plasma spraying

Table 2 Plasma spraying parameters for YSB deposition

Spray parameter	Unit	Value
Spray distance	mm	80
Plasma arc power	kW	25
Primary plasma gas (Ar)	L min ⁻¹	45
Auxiliary plasma gas (H ₂)	L min ⁻¹	2

Characterization Methods

The phase structures of the YSB deposits were characterized by x-ray diffraction (XRD, D8 ADVANCE, Bruker) analysis. The microstructure of the YSB deposits was examined from the both polished cross sections and fractured cross sections by scanning electron microscopy (SEM, MIRA 3 LMH, TESCAN, Czech). The porosity in the deposit was estimated by image analyzing method using SEM images taken in the BEI mode from the polished cross sections, while the fractured cross sections were used to reveal the lamellar interface bonding state since weak interface bonding can be highlighted through fracturing stress. The energy-dispersive spectroscopy (EDS) was used for the quantitative analysis of elements in the samples. The impedance analysis was used to measure the conductivity of deposits at a temperature range of 350–750 °C using free-standing YSB deposits with the silver paste on both sides. The measurement was performed by Solatron Electrochemical Analysis Station (SI 1260/1287) with a frequency range from 0.1 to 100 kHz and 25 mV AC bias.

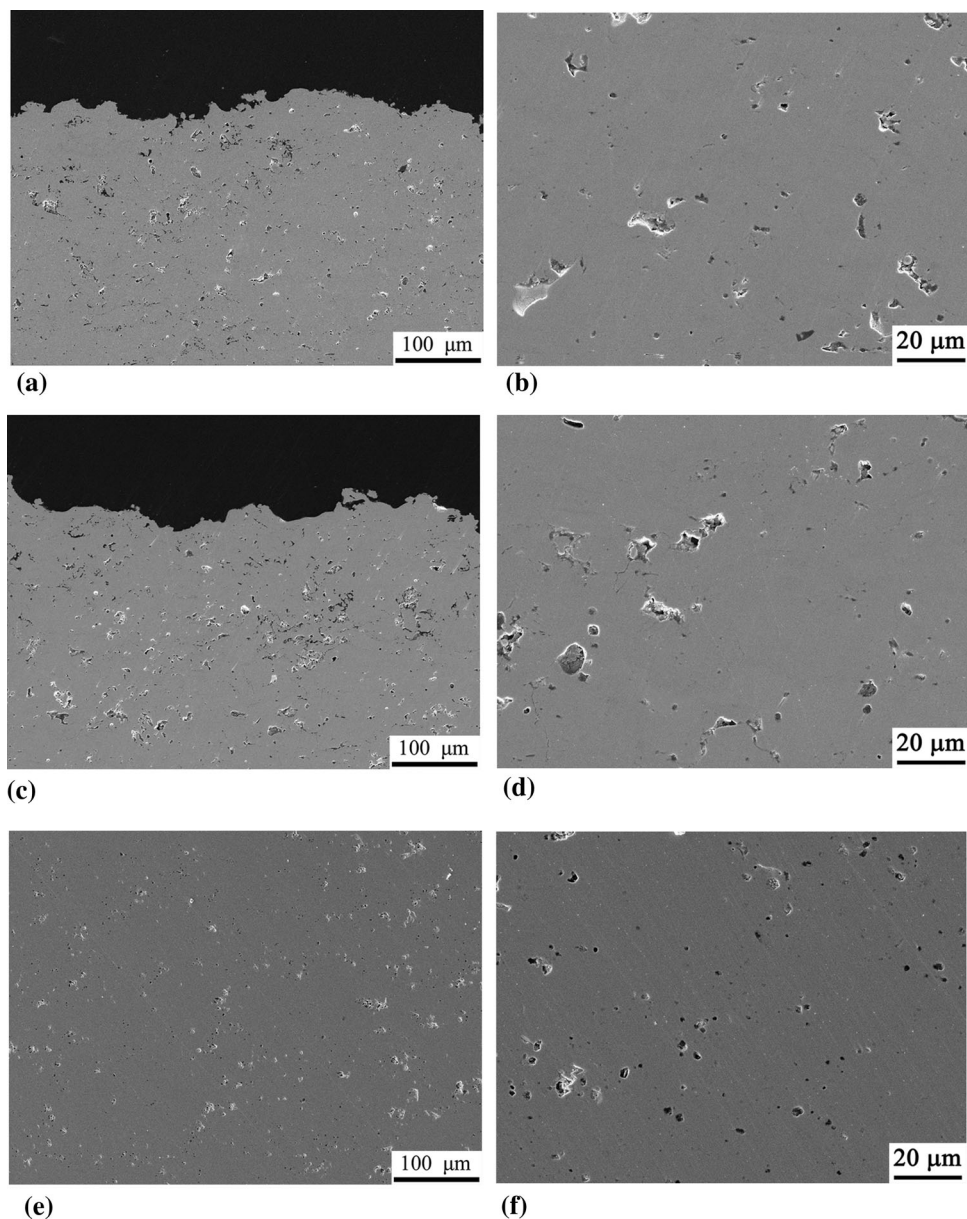
Results and Discussion

Microstructure of Plasma-Sprayed YSB Deposits

Figure 3 shows the cross-sectional microstructures of the polished YSB deposits plasma sprayed at room temperature and 350 °C, and YSB sintered pellet. From Fig. 3(a) and (b) it can be observed that no evident unbounded lamellar interface, through-thickness pores, and visible cracks are present in the deposit sprayed at 350 °C. As shown in Fig. 3(a) and (c), the deposit fabricated at 350 °C is denser than that obtained at room temperature. Compared with the cross-sectional microstructure of the polished sintered YSB pellet as shown in Fig. 3(e) and (f), the pores in the deposits are a little larger than those in the sintered pellet. The image analyzing method was used to estimate the porosity of samples from the cross-sectional images. The quantitative analysis yielded the porosity levels of $2.2 \pm 0.1 \%$, $3.6 \pm 0.5 \%$, and $4.3 \pm 0.5 \%$ for the sintered pellet, the deposits at 350 °C and room temperature, respectively. As shown in Fig. 3(a), (b), (c) and (d), the three-dimensional pores with globe and irregular shape in sizes from submicrometers to several micrometers were observed in both deposits sprayed at two deposition temperatures. The formation of globe pores is possibly retained from the gas phase enclosed in feedstock powder particle during the solidification process (Ref 32). Besides those globe pores, pores with irregular shape can be related to the incomplete filling and infiltration during the spreading of molten droplets.

The fractured cross-section morphology can be utilized for the visualization of the interlamellar bonding condition of the plasma-sprayed ceramic coating. Figure 4 shows the morphology of the fractured surface of both of the deposits sprayed at room temperature and 350 °C. As can be seen from the morphologies of the fractured surface shown in Fig. 4(a), (b), (d) and (e), which is consistent with the results in Fig. 3(a), (b), (c) and (d), pores with globe and irregular shape were observed in the deposits. Both of the deposits sprayed at two different temperatures did not present the evident fracture from weakly bonded lamellar interfaces, indicating that lamellae were well bonded in the as-sprayed state. As shown in Fig. 4(a) and (d), the plasma-sprayed YSBs present distinctly different microstructure features from the conventional one. In particular for the deposit deposited at 350 °C, as shown in Fig. 4(b) and (c), it is even difficult to observe the conventional lamellar structural features, and the morphology of fractured surface is similar to that of the sintered bulk ceramics, indicating that the lamellae in the YSB deposit sprayed at 350 °C were fully bonded together. For the YSB electrolyte deposited at room temperature, occasionally, several

Fig. 3 Cross-sectional microstructures of free-standing plasma-sprayed YSB coatings deposited at 350 °C: (a), and (b) and room temperature: (c), and (d); cross-sectional microstructures of YSB sintered pellet: (e), and (f)



interfaces between lamellae were still distinctly observed on the fractured surface in Fig. 4(e), and a trace of ambiguous lamellar structure feature and the columnar grains grew through several lamellae with a length of about 4–5 μm were observed on the fractured surface as shown in Fig. 4(f). The result reveals that the molten droplets nucleate heterogeneously on the previously deposited splat particles during the solidification process, which leads to the formation of the columnar microstructure across several lamellae (Ref 33). Thus, increasing the deposition temperature improves the formation of interlamellar bonding. Accordingly, a dense fully bonded YSB electrolyte can be deposited by using APS.

Phase Structures of Plasma-sprayed YSB Deposits

Figure 5 shows the XRD patterns of the YSB deposits sprayed at two different deposition temperatures. The phases of two electrolyte deposits are summarized in Table 3. It can be found that the electrolyte deposited at room temperature showed the diffraction peaks of the cubic fluorite structure δ -phase with the Fm-3m space group (PDF #27-1047), metastable III-phase with P1 space group (PDF #50-1088), and traces of peaks from the tetragonal β -phase with P-421c space group (PDF #27-0050). However, when the deposition temperature was increased from room temperature to 350 °C, only the peaks of δ -phase were observed.

Fig. 4 Morphology of the fractured plasma-sprayed YSB coatings deposited at 350 °C: (a), (b), and (c), and room temperature: (d), (e), and (f)

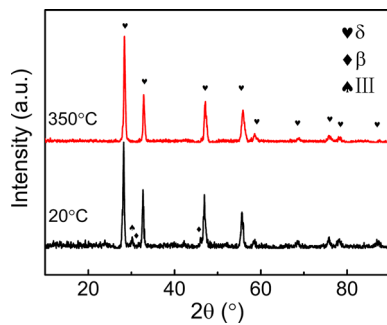
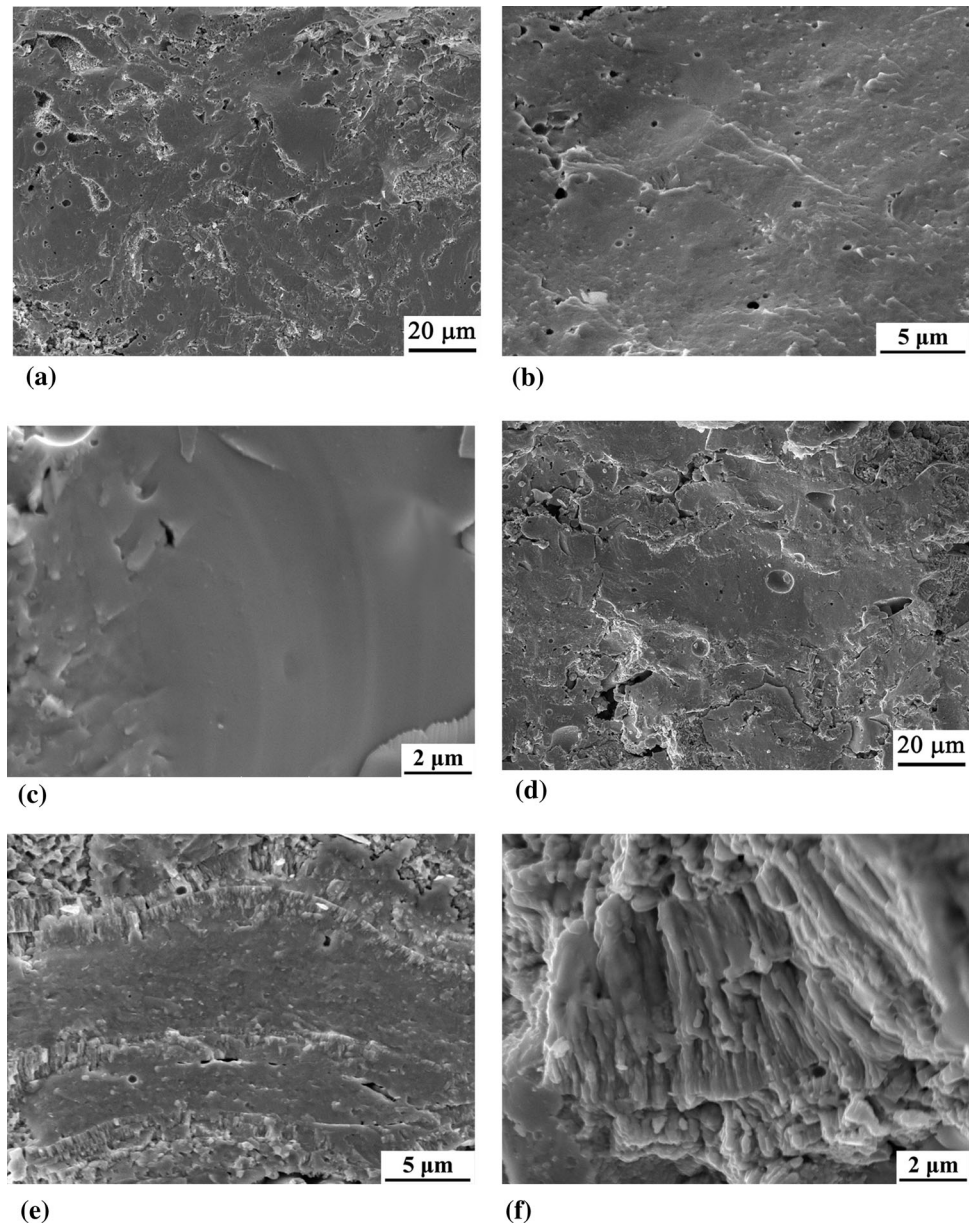


Fig. 5 The XRD patterns of YSB coatings deposited at both 350 °C and the room temperature

The formation of various phases in the YSB deposit can be attributed to the vaporization of bismuth during plasma spraying. It was reported that during plasma spraying of multi-component ceramic material the component with a high vapor pressure or low boiling point evaporates preferentially (Ref 23, 28-30). When YSB powder particles are fed into high-temperature plasma jet, YSB spray particles are rapidly heated to the molten state. Then, the Bi_2O_3 evaporates from the droplet surface more rapidly compared with Y_2O_3 due to its higher vapor pressure and subsequently, the relative concentration of Y_2O_3 is increased in YSB molten droplet. As shown in Table 4, in the plasma-sprayed YSB deposit, the percentage of Y^{3+} average concentration increased from 24.7% in the powder to

Table 3 Phases in the plasma-sprayed YSB deposits

YSB deposit sprayed at 350 °C	YSB deposit sprayed at room temperature
δ	$\delta, \beta, \text{III}$

Table 4 Cations percentage of YSB powder and deposit

Element, %	Powder	Deposit
Y^{3+}	24.7	29.4
Bi^{3+}	75.3	70.6
Total	100	100

29.4% in the deposit. This fact shows that the bismuth oxide with a higher vapor pressure than Y_2O_3 tends to preferentially evaporate during plasma spraying of YSB. The significant reduction of Bi_2O_3 content in YSB could lead to new phase formation. At a low deposition temperature, the spreading liquid splat tends to solidify more rapidly. The inhomogeneous distribution of the Y element in the molten droplet results in the formation of III-phase with a relatively high Y_2O_3 concentration, accompanying with the formation of a small fraction of β -phase. It can be considered that at the high deposition temperature, a significant lower solidification rate promotes the diffusion of elements in droplets, which further favors the formation of uniform δ -phase. Consequently, III-phase and β -phase peaks on XRD patterns in the YSB deposit sprayed at 350 °C disappeared. As a result, on the XRD pattern of the YSB deposit sprayed at 350 °C, only the peaks of δ -phase were observed.

Therefore, it is clear that the present results show that the crystalline structure of plasma-sprayed YSB is influenced by the deposition temperature. Due to the significant difference in the low melting point of Bi_2O_3 as compared to Y_2O_3 , a certain level of Bi_2O_3 loss during plasma spraying is inevitable. To deposit the YSB without lower conducting phase, it is necessary to increase the deposition temperature.

Ionic Conductivity of Plasma-sprayed YSB electrolyte

The ionic conductivities of the free-standing YSB deposits and sintered YSB bulk pellet measured in air against the temperature are shown in Fig. 6. The plots reveal that the conductivity increases with test temperature. The sintered YSB bulk exhibits the ionic conductivities of $2.1 \times 10^{-1} \text{ S cm}^{-1}$ at 700 °C and $1.3 \times 10^{-2} \text{ S cm}^{-1}$ at 500 °C, being similar to those reported previously for YSB materials (Ref 14). The YSB electrolyte deposited at room temperature exhibits the ionic conductivity of $1.5 \times 10^{-1} \text{ S cm}^{-1}$ at 700 °C and $3.6 \times 10^{-3} \text{ S cm}^{-1}$ at 500 °C, while the electrolyte deposited at 350 °C exhibits the ionic conductivity of

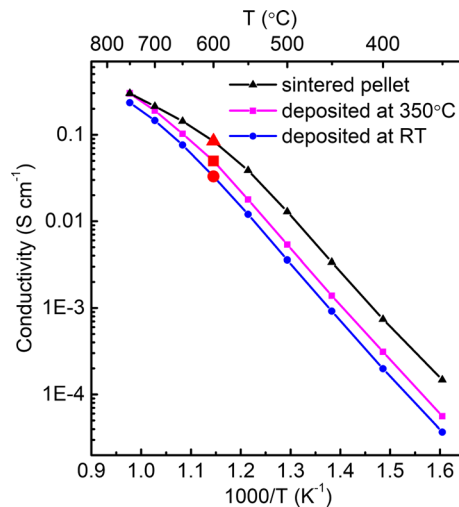


Fig. 6 The temperature dependence of the ion conductivity of sintered YSB pellet and plasma-sprayed YSB samples at 350 °C and room temperature

$1.9 \times 10^{-1} \text{ S cm}^{-1}$ at 700 °C and $5.4 \times 10^{-3} \text{ S cm}^{-1}$ at 500 °C. The difference in ionic conductivity between plasma-sprayed YSB electrolyte and sintered pellets can be attributed to the higher Y^{3+} content and microstructure. The conductivity of the YSB electrolyte deposited at room temperature is lower than electrolyte deposited at 350 °C. This difference can be mainly attributed to the difference in the microstructure and higher porosity in the YSB deposited at room temperature. The 700 °C conductivity of YSB plasma sprayed at 350 °C reached 90% of the sintered bulk pellet, while the 500 °C conductivity of YSB electrolyte plasma sprayed at 350 °C accounts for 42% of the sintered bulk pellet. The relatively high ionic conductivity of plasma-sprayed YSB at a high-temperature region can be attributed to the oxygen transportation mechanism which is associated with the high Y_2O_3 content.

As shown in Fig. 6, a knee point (the highlight red mark) is present in the ionic conductivity curves of YSB electrolytes at about 600 °C, corresponding to the change of activation energy for oxygen ion conduction. The change of activation energies suggests two different ion conducting mechanisms in different temperature ranges, which are corresponded to two defect structures in YSB, since it was reported that the YSB undergoes an order-disorder transition of the oxygen sublattice at about 600 °C (Ref 9). At the temperature range lower than 600 °C, the diffuse scattering result of neutron diffraction indicates that the ordered oxygen vacancies are present in the oxygen sublattice (Ref 34). When the temperature is increased over 600 °C, the

Table 5 Activation energy of YSB samples

YSB	Activation energy, eV	
	> 600 °C	< 600 °C
Coating deposited at room temperature	0.92	1.29
Coating deposited at 350 °C	0.88	1.28
Sintered pellet	0.62	1.25

lattice transforms into disorders and all oxygen ions take part in the conductivity process, and the lattice behaves “ δ - Bi_2O_3 like.”

As can be seen in Fig. 6, the ionic conductivity curves of two YSB deposits showed the less distinct knee point around 600 °C as compared to that observed for sintered bulk, which corresponds to the limited changes of the activation energies compared with sintered bulk shown in Table 5. The fact that the conductivity at the temperature range higher than 600 °C was increased in the same fashion of low temperature range suggests that for plasma-sprayed YSB deposits part of order oxygen vacancies in the lattice is maintained to higher temperature. As a result, the stability of oxygen sublattice ordering of the plasma-sprayed YSBs is enhanced. It was reported that above 600 °C, the activation energy of $(\text{Bi}_2\text{O}_3)_{1-x}(\text{Ln}_2\text{O}_3)_x$ ($\text{Ln} = \text{Y}, \text{Gd}, \text{Dy}, \text{Er}$) increases with increasing x (Ref 9). This is because the migration ability of the mobile oxygen ions strongly decreases with the increase in the Y^{3+} concentration which results in the increase in activation energy at the high temperature. Therefore, the enhanced stability of oxygen sublattice ordering in plasma-sprayed YSZ can be attributed to the increased Y^{3+} content.

Summary

In this study, using YSB spray powders with stable δ -phase synthesized by sinter-crushing reaction, dense YSB electrolyte with sufficiently bonded lamellae was deposited by APS. The plasma-sprayed YSB presented a similar dense structure to that of sintered bulk although a small amount of unbonded lamellar interfaces were observed. It was found that the phase structure of the YSB deposit was influenced by deposition temperature. The YSB with a stable δ -phase was deposited at the deposition temperature of 350 °C. Results showed that the plasma-sprayed YSB electrolyte with fully bonded lamellae and pure cubic δ -phase deposited at 350 °C presents high ion conductivity of $1.9 \times 10^{-1} \text{ S cm}^{-1}$ at 700 °C and $5.4 \times 10^{-3} \text{ S cm}^{-1}$ at 500 °C in comparison with $2.1 \times 10^{-1} \text{ S cm}^{-1}$ at 700 °C and $1.3 \times 10^{-2} \text{ S cm}^{-1}$ at 500 °C for sintered bulk. The

relativity high conductivity at high temperature, corresponding to the high activation energies of the deposits at high-temperature region, is related to the higher Y^{3+} content of plasma-sprayed YSB. The high conductivity feature indicates that bismuth oxide-based electrolytes fabricated by atmospheric plasma spraying are of great potential for manufacturing of the IT-SOFC.

Acknowledgments The present project is financially supported by The National Key Research and Development Program of China (No. 2017YFE0105900).

References

1. S.C. Singhal, Advances in Solid Oxide Fuel Cell Technology, *Solid State Ion*, 2000, **135**(1), p 305-313.
2. E.D. Wachsman and K.T. Lee, Lowering the Temperature of Solid Oxide Fuel Cells, *Science*, 2011, **334**, p 934-939.
3. B. Scrosati, A. Magistris, C.M. Mari and G. Mariotto, *In Fast Ion Transport in Solids*, Springer, Dordrecht , 1993.
4. N.M. Sammes, G.A. Tompsett, H. Nafe and F. Aldingera, Bismuth Based Oxide Electrolytes-Structure and Ionic Conductivity, *J. Eur. Ceram. Soc.*, 1999, **19**(10), p 1801-1826.
5. R. O'Hayre, S.-W. Cha, W.G. Colella and F.B. Prinz, *Fuel Cell Fundamentals*, Springer, Berlin, 2009.
6. R. Sachitanand, M. Sattari, J.-E. Svensson, J. Froitzheim (2013) Evaluation of the Oxidation and Cr Evaporation Properties of Selected FeCr Alloys Used as SOFC Interconnects. *Int. J. Hydrogen Energy*; 38:15328-15334
7. P. Shuk, H.-D. Wiemhöfer, U. Guth, W. Gopel and M. Greenblatt, Oxide Ion Conducting Electrolytes Based on Bi_2O_3 , *Solid State Ionics*, 1996, **89**(3-4), p 179-196.
8. A. Laarif and F. Theobald, The Lone Pair Concept and the Conductivity of Bismuth Oxides Bi_2O_3 , *Solid State Ion.*, 1986, **21**(3), p 183-193.
9. M.J. Verkerk and A.J. Burggraaf, High Oxygen Ion Conduction in Sintered Oxides of the Bi_2O_3 - Dy_2O_3 System, *J. Electrochem. Soc.*, 1981, **128**(1), p 75-82.
10. M.J. Verkerk, K. Keizer and A.J. Burggraaf, High Oxygen Ion Conduction in Sintered Oxides of the Bi_2O_3 - Er_2O_3 System, *J. Appl. Electrochem.*, 1980, **10**(1), p 81-90.
11. K.V. Kale, K.M. Jadhav and G.K. Bichile, Investigations on a High-conductivity Solid Electrolyte System, Bi_2O_3 - Y_2O_3 , *J. Mater. Sci. Lett.*, 1999, **18**(1), p 9-11.
12. K.Z. Fung, J. Chen and A.V. Virkar, Effect of Aliovalent Dopants on the Kinetics of Phase Transformation and Ordering in RE_2O_3 - Bi_2O_3 ($\text{RE} = \text{Yb}, \text{Er}, \text{Y}, \text{or Dy}$) Solid Solutions, *J. Amer. Chem. Soc.*, 1993, **76**(10), p 2403-2418.
13. S.E. Lin and W.C.J. Wei, Long-term Degradation of Ta_2O_5 -Doped Bi_2O_3 Systems, *J. Eur. Ceram. Soc.*, 2011, **31**(16), p 3081-3086.
14. T. Takahashi, H. Iwahara and T. Arao, High Oxide Ion Conducting in Sintered Oxides of the System Bismuth Bi_2O_3 - Y_2O_3 , *J. Appl. Electrochem.*, 1975, **5**, p 187-195.
15. J.S. Ahn, M.A. Camaratta, K.T. Lee, H. Yoon, B.W. Lee and E.D. Wachsman, High Performance Ceria/Bismuth Oxide Bilayered Electrolyte IT-SOFC, *Electrochem. Commun.*, 2009, **16**(51), p 1504-1507.
16. S.G. Kim, S.P. Yoon, S.W. Nam, S.H. Hyun and S.A. Hong, Fabrication and Characterization of a YSZ/YDC Composite Electrolyte by a Sol-gel Coating Method, *J. Power Sources*, 2002, **110**(1), p 222-228.

17. J.Y. Park, H. Yoon and E.D. Wachsman, Fabrication and Characterization of High-Conductivity Bilayer Electrolytes for Intermediate-Temperature Solid Oxide Fuel Cells, *J. Amer. Chem. Soc.*, 2005, **88**(9), p 2402-2408.
18. Z.P. Shao and S.M. Haile, A High Performance Cathode for the Next Generation Solid-Oxide Fuel Cells, *Nature*, 2004, **431**, p 170-173.
19. A. Casanova, A Consortium Approach to Commercialized Westinghouse Solid Oxide Fuel Cell Technology, *J. Power Sources*, 1998, **71**(1-2), p 65-70.
20. L. Zhang, C. Xia, F. Zhao and L.-F. Chen, Thin Film Ceria-Bismuth Bilayer Electrolytes for Intermediate Temperature Solid Oxide Fuel Cells with $\text{La}_{0.85}\text{Sr}_{0.15}\text{MnO}_{3-\delta}\text{Y}_{0.25}\text{Bi}_{0.75}\text{O}_{1.5}$ Cathodes, *Mater. Res. Bull.*, 2010, **45**(5), p 603-608.
21. W.M. Guo, J. Liu and C. Jin, Anode-Supported LaGaO_3 -Based Electrolyte SOFCs with Y_2O_3 -Doped Bi_2O_3 and La-Doped CeO_2 Buffer Layers, *J. Alloys Compd.*, 2010, **504**(2), p 21-24.
22. S.-L. Zhang, C.-X. Li and C.-J. Li, Plasma-Sprayed Y_2O_3 -Stabilized ZrO_2 Electrolyte With Improved Interlamellar Bonding for Direct Application to Solid Oxide Fuel Cells, *J. Fuel Cell Sci. Technol.*, 2014, **11**(3), p 031005.
23. S.-L. Zhang, T. Liu, C.-J. Li, S.-W. Yao, C.-X. Li, G.-J. Yang and M. Liu, Atmospheric Plasma-sprayed $\text{La}_{0.8}\text{Sr}_{0.2}\text{Ga}_{0.8}\text{Mg}_{0.2}\text{O}_3$ Electrolyte Membranes for Intermediate-Temperature Solid Oxide Fuel Cells. *J. Mater. Chem. A*, 2015, **3**, p 7535-7553.
24. C.-J. Li, G.J. Yang and C.X. Li, Development of Particle Interface Bonding in Thermal Spray Coatings: A Review, *J. Therm. Spray Technol.*, 2013, **22**(2-3), p 192-206.
25. G.-J. Yang, C.-X. Li, S. Hao, Y.-Z. Xing, Y.-Z. Xing and C.-J. Li, Critical Bonding Temperature for the Splat Bonding Formation During Plasma Spraying of Ceramic Materials, *Surf. Coat. Technol.*, 2013, **235**, p 841-847.
26. S.-W. Yao, C.-J. Li, J.-J. Tian, G.-J. Yang and C.-X. Li, Conditions and Mechanisms for the Bonding of a Molten Ceramic Droplet to a Substrate after High-speed Impact, *ACTA Mater.*, 2016, **119**, p 9-25.
27. C.-J. Li, Q.-L. Zhang, S.-W. Yao, G.-J. Yang and C.-X. Li, Plasma Spraying of Dense Ceramic Coating with Fully Bonded Lamellae through Materials Design Based on the Critical Bonding Temperature Concept, *J. Therm. Spray Technol.*, 2019, **28**, p 53-62.
28. G. Mauer, D. Sebold, R. Vaßen and D. Stover, Improving Atmospheric Plasma Spraying of Zirconate Thermal Barrier Coatings Based on Particle Diagnostics, *J. Therm. Spray Technol.*, 2012, **21**(3-4), p 363-371.
29. X. Chen, C.-C. Kou, S.-L. Zhang, C.-X. Li, G.-J. Yang and C.-J. Li, Effects of Powder Structure and Size on Gd_2O_3 Preferential Vaporization During Plasma Spraying of $\text{Gd}_2\text{Zr}_2\text{O}_7$, *J. Therm. Spray Technol.*, 2019, **29**(8), p 105-114.
30. X. Chen, S.-L. Zhang, C.-X. Li and C.-J. Li, Optimization of Plasma-Sprayed Lanthanum Chromite Interconnector Through Powder Design and Critical Process Parameters Control, *J. Therm. Spray Technol.*, 2019, **29**(3), p 212-222.
31. M. Marchetti, M. Valérie, R. Pitre, S. Datcu, L. Ibos and J. Livet, Emissivity Measurements of Road Materials, 2004 Quantitative InfraRed Thermography, *Quant Infr Therm J.*, 2004, **1**(1), p 1.2.1-7.
32. E.-J. Yang, G.-J. Yang, X.-T. Luo, C.-J. Li and M. Takahashi, Epitaxial Grain Growth During Splat Cooling of Alumina Droplets Produced by Atmospheric Plasma Spraying, *J. Therm. Spray Technol.*, 2013, **22**(2), p 152-157.
33. A. Ohmori and C.-J. Li, Quantitative Characterization of the Structure of Plasma-Sprayed Al_2O_3 Coating by Using Copper Electroplating, *Thin Solid Films*, 1991, **201**(2), p 241-252.
34. S. Boyapati, E.D. Wachsman and B.C. Chakoumakos, Neutron Diffraction Study of Occupancy and Positional order of Oxygen Ions in Phase Stabilized Cubic Bismuth Oxides, *Solid State Ion*, 2001, **138**(3-4), p 293-304.

Publisher's Note Springer Nature remains neutral with regard to jurisdictional claims in published maps and institutional affiliations.